Selective Synthesis of Hollow and Filled Fullerene-like (IF) WS_2 Nanoparticles via Metal–Organic Chemical Vapor Deposition

Nicole Zink,[†] Julien Pansiot,[†] Jérôme Kieffer,[†] Helen Annal Therese,[†] Martin Panthöfer,[†]
Frank Rocker,[†,‡] Ute Kolb, and Wolfgang Tremel*,[†]

Institut für Anorganische Chemie and Analytische Chemie, Johannes Gutenberg-Universität Mainz, Duesbergweg 10-14, D-55099 Mainz, Germany, and Institut für Physikalische Chemie, Johannes Gutenberg-Universität Mainz, Welderweg 11, D-55099 Mainz, Germany

Received April 4, 2007. Revised Manuscript Received October 23, 2007

The synthesis of WS_2 onion-like nanoparticles by means of a high-temperature metal–organic chemical vapor deposition (MOCVD) process starting from $W(CO)_6$ and elemental sulfur is reported. The reaction can be carried out as a single-step reaction or in a two-step process where the intermediate products, amorphous WS_2 nanoparticles, formed through the high-temperature reaction of tungsten and sulfur in the initial phase of the reaction, are isolated and converted into onion-type WS_2 nanoparticles in a separate annealing step. Analysis of the reaction product using X-ray diffraction (XRD) and high-resolution transmission electron microscopy (HRTEM) combined with energy dispersive X-ray spectroscopy (EDX) allowed to optimize the reaction in such a way that filled onion-like structures are formed in a one-step reaction, whereas hollow onion-like structures are obtained by the two-step procedure. A model could be devised that allows us to rationalize the different outcome of the reactions. The MOCVD approach therefore allows a selective synthesis of open and filled fullerene-like chalcogenide nanoparticles.

Introduction

Most of the transition metal chalcogenides, MQ_2 ($M =$ group 4–7 metal; $Q =$ S, Se, Te), display a characteristic layered structure. MQ_2 slabs are formed by two layers of close-packed chalcogenide atoms sandwiching one metal layer between them. These slabs are stacked, with van der Waals forces between the slabs only. The metal coordination may vary depending on M; while group 4, 5, and 7 metals prefer octahedral coordination geometry, a trigonal-prismatic coordination is adopted by the group 6 metals Mo and W, which is directly related to the semiconducting properties of MoS_2 and WS_2.[1,2] The steric shielding of the metal atoms by the chalcogenide layers combined with the semiconducting properties make MoS_2 and WS_2 so inert that (in contrast to the II–VI semiconductors or TiS_2) they resist oxidation even in moist air at temperatures close to 100 °C[3] and make them interesting materials in the fields of catalysis, electrocatalysis, electrochemical intercalation, and solid lubrication.

As in other layered compounds such as graphite[4] or boron nitride,[5] the instability of the weakly van der Waals bonded slabs against folding and the need to saturate dangling bonds at the layer edges lead to the formation of spherical or cylindrical particles, in contrast to the flat crystalline polymorphs.[6] A characteristic feature of closed-shell MQ_2-derived structures is that they are only metastable phases at room temperature because high preparation temperatures ($>$800 °C) are needed in order to interconnect the edges of single MQ_2 layers through the formation of rhomboidal and triangular point defects which provide curvature to the otherwise flat 2D MQ_2 slabs. Tenne and co-workers were the first to show that fullerene-type nanoparticles or nanopolyhedra and nanotubes represent an integral part of the phase diagram of MoS_2 and WS_2.[7] In the following decade a variety of methods including arc discharge,[8,9] sulfurization/selenization of metal oxides,[10–20] chlorides,[21,22] or carbon-

---

* Corresponding author: Tel +49-6131-392-5135; Fax +49-6131-392-5605; e-mail tremel@uni-mainz.de.

[†] Institut für Anorganizche Chemie and Analytische Chemie.

[‡] Institut für Physikalische Chemie.

(1) Tremel, W.; Seshadri, R.; Finckh, E. W. *Chem. Unserer Zeit* **2001**, *35*, 42.
(2) Tremel, W.; Finckh, E. W. *Chem. Unserer Zeit* **2004**, *38*, 326.
(3) Ross, S.; Sussman, A. *J. Phys. Chem.* **1955**, *59*, 889.
(4) Kroto, H. W.; Heath, J. R.; O'Brien, S. C.; Curl, R. F.; Smalley, R. E. *Nature (London)* **1985**, *318*, 162.
(5) Chopra, N. G.; Luyken, R. J.; Cherrey, K.; Crespi, V. H.; Cohen, M. L.; Louie, S. G.; Zettl, A. *Science* **1995**, *269*, 966.
(6) Tremel, W. *Angew. Chem., Int. Ed. Engl.* **1999**, *38*, 2175.
(7) Tenne, R.; Margulis, L.; Genut, M.; Hodes, G. *Nature (London)* **1992**, *360*, 444.
(8) Alexandrou, I.; Sano, N.; Burrows, A.; Meyer, R. R.; Wang, H.; Kirkland, A. I.; Kiely, C. J.; Amaratunga, G. A. J. *Nanotechnology* **2003**, *14*, 913.
(9) Hu, J. J.; Bultman, J. E.; Zabinski, J. S. *Tribol. Lett.* **2004**, *17*, 543.
(10) Camacho-Bragado, G. A.; Elechiguerra, J. L.; Olivas, A.; Fuentes, S.; Galvan, D.; Yacaman, M. J. *J. Catal.* **2005**, *234*, 182.
(11) Chen, W. X.; Tu, J. P.; Ma, X. C.; Xu, Z. D.; Tenne, R.; Rosenstveig, R. *Chin. Chem. Lett.* **2003**, *14*, 312.
(12) Feldman, Y.; Frey, G. L.; Homyonfer, M.; Lyakhovitskaya, V.; Margulis, L.; Cohen, H.; Hodes, G.; Hutchison, J. L.; Tenne, R. *J. Am. Chem. Soc.* **1996**, *118*, 5362.
(13) Feldman, Y.; Margulis, L.; Homyonfer, M.; Tenne, R. *High. Temp. Mater. Proc.* **1996**, *15*, 163.
(14) Feldman, Y.; Zak, A.; Popovitz-Biro, R.; Tenne, R. *Solid State Sci.* **2000**, *2*, 663.
(15) Zak, A.; Feldman, Y.; Alperovich, V.; Rosentsveig, R.; Tenne, R. *J. Am. Chem. Soc.* **2000**, *122*, 11108.
(16) Li, X. L.; Li, Y. D. *Chem.—Eur. J.* **2003**, *9*, 2726.
(17) Rothschild, A.; Tenne, R.; Sloan, J.; York, A. P. E.; Green, M. L. H.; Sloan, J.; Hutchison, J. L. *Chem. Commun.* **1999**, 363.
(18) Tsirlina, T.; Feldman, Y.; Homyonfer, M.; Sloan, J.; Hutchison, J. L.; Tenne, R. *Fullerene Sci. Technol.* **1998**, *6*, 157.
(19) Whitby, R. L. D.; Hsu, W. K.; Lee, T. H.; Boothroyd, C. B.; Kroto, H. W.; Walton, D. R. M. *Chem. Phys. Lett.* **2002**, *359*, 68.

10.1021/cm070938s CCC: \$37.00

yls,[23] decomposition of ammonium thiometallates,[24–27] chemical vapor transport,[28,29] laser ablation,[30–33] microwave plasma,[34,35] atmospheric pressure chemical vapor deposition (APCVD),[22,36] metal–organic chemical vapor deposition (MOCVD),[37] and spray pyrolysis[38] were utilized for the synthesis of inorganic fullerene (IF)- or nanotube-like (NT) structures of MQ_2 materials.

These nanostructures are interesting not only as model systems to overcome the gap between the chemistry at the atomic/molecular level and that of bulk compounds or as playground for research on quantum confinement effects[39] but also for diverse applications in engineering (e.g., as lubricants[40–46] with antiwear effect,[47] as highly shock-wave-resistant materials,[48,49] or energy industry (e.g., photovoltaic films,[50] material for H_2 storage,[51,52] electrode material in lithium batteries,[52–54] or for catalysis[10,55–58]).

A particular problem in the synthesis of WS_2 fullerene-type nanoparticles and nanotubes is that they are high-temperature and low-pressure phases in the W–S diagram which are not accessible by traditional solid-state synthesis. In conventional high-temperature reactions the energy required for the solid-state diffusion of the reactants would exceed the nucleation energy of the metastable WS_2 nanoparticles. A consequence of these bulk reactions is that only the thermodynamically most stable final products, i.e., 2H-WS_2 in the present case, can be produced. In contrast, reactions that are kinetically controlled, i.e., where solid-state diffusion is not crucial, a phase may nucleate and grow until its growth exhausts the supply of the reactants. The sequence of phases formed depends upon the relative activation energies for nucleation of the various compounds, and compounds in the equilibrium phase diagram may be temporarily skipped if they have a large activation energy for nucleation. In fact, all synthetic approaches to chalcogenide nanoparticles mentioned above rely on the minimization of solid-state diffusion.

Our approach to suppress solid-state diffusion as a reaction parameter is based on a gas-phase MOCVD reaction. In a recent communication we have described the gas-phase synthesis of MoS_2 and $MoSe_2$ hollow IF particles by using a two-step MOCVD-based reaction.[37] In the first synthetic step chalcogenide nanoparticles are formed in a gas-phase reaction between Mo, produced by thermal decomposition of $Mo(CO)_6$, and sulfur or selenium, respectively. One might speculate that in a subsequent growth step the lamellar sheet fragments continue to grow and begin to loosen at their ends until they roll up into onion-type structures. The particular advantages of this method are that (i) the generalized procedure might be extended to other members of the MQ_2 group, provided that volatile precursors are available, (ii) the synthesis of solid solutions $M_{1-x}M'_xQ_2$ or $MQ_{1-x}Q'_x$ or even ternary phases may be envisioned, (iii) a study of the initial phases of the reaction with sophisticated in situ techniques could be done, but (iv) still the reaction can be stopped at any time in order to perform a time-dependent structural investigation of the reaction products. (v) The procedure may be scaled up for the synthesis of large quantities by parallelization with the aid of microreactors, (vi) the use of highly toxic reactants H_2S and H_2Se is avoided, and (vii) a facile and fast synthesis of selenides (and even tellurides) without the thermally labile H_2Se (H_2Te) is possible in quantitative amounts.

---

(20) Coleman, K. S.; Sloan, J.; Hanson, N. A.; Brown, G.; Clancy, G. P.; Terrones, M.; Terrones, H.; Green, M. L. H. *J. Am. Chem. Soc.* **2002**, *124*, 11580.
(21) Margolin, A.; Popovitz-Biro, R.; Albu-Yaron, A.; Moshkovich, A.; Rapoport, L.; Tenne, R. *Curr. Nanosci.* **2005**, *1*, 253.
(22) Schuffenhauer, C.; Popovitz-Biro, R.; Tenne, R. *J. Mater. Chem.* **2002**, *12*, 1587.
(23) Lee, G. H.; Jeong, J. W.; Huh, S. H.; Kim, S. H.; Choi, B. J.; Kim, Y. W. *Int. J. Mod. Phys. B* **2003**, *17*, 1134.
(24) Zelenski, C. M.; Dorhout, P. K. *J. Am. Chem. Soc.* **1998**, *120*, 734.
(25) Chen, J.; Li, S.-L.; Gao, F.; Tao, Z.-L. *Chem. Mater.* **2003**, *15*, 1012.
(26) Nath, M.; Govindaraj, A.; Rao, C. N. R. *Adv. Mater.* **2001**, *13*, 283.
(27) Rao, C. N. R.; Nath, M. *Dalton Trans.* **2003**, 1.
(28) Remskar, M.; Mrzel, A.; Skraba, Z.; Jesih, A.; Ceh, M.; Demsar, J.; Stadelmann, P.; Levy, F.; Mihailovic, D. *Science* **2001**, *292*, 479.
(29) Remskar, M.; Skraba, Z.; Regula, M.; Ballif, C.; Sanjines, R.; Levy, F. *Adv. Mater.* **1998**, *10*, 246.
(30) Parilla, P. A.; Dillon, A. C.; Parkinson, B. A.; Jones, K. M.; Alleman, J.; Riker, G.; Ginley, D. S.; Heben, M. J. *J. Phys. Chem. B* **2004**, *108*, 6197.
(31) Hacohen, Y. R.; Popovitz-Biro, R.; Prior, Y.; Gemming, S.; Seifert, G.; Tenne, R. *Phys. Chem. Chem. Phys.* **2003**, *5*, 1644.
(32) Sen, R.; Govindaraj, A.; Suenaga, K.; Suzuki, S.; Kataura, H.; Iijima, S.; Achiba, Y. *Chem. Phys. Lett.* **2001**, *340*, 242.
(33) Schuffenhauer, C.; Parkinson, B. A.; Jin-Phillipp, N. Y.; Joly-Pottuz, L.; Martin, J.-M.; Popovitz-Biro, R.; Tenne, R. *Small* **2005**, *1*, 1100.
(34) Vollath, D.; Szabo, D. V. *Mater. Lett.* **1998**, *35*, 236.
(35) Vollath, D.; Szabo, D. V. *Acta Mater.* **2000**, *48*, 953.
(36) Li, X.-L.; Ge, J.-P.; Li, Y.-D. *Chem.—Eur. J.* **2004**, *10*, 6163.
(37) Etzkorn, J.; Therese, H. A.; Rocker, F.; Zink, N.; Kolb, U.; Tremel, W. *Adv. Mater.* **2005**, *17*, 2372.
(38) Bastide, S.; Duphil, D.; Borra, J.-P.; Levy-Clement, C. *Adv. Mater.* **2006**, *18*, 106.
(39) Chikan, V.; Kelley, D. F. *J. Phys. Chem. B* **2002**, *106*, 3794.
(40) Rapoport, L.; Bilik, Y.; Feldman, Y.; Homyonfer, M.; Cohen, S. R.; Tenne, R. *Nature (London)* **1997**, *387*, 791.
(41) Chhowalla, M.; Amaratunga, G. A. J. *Nature (London)* **2000**, *407*, 164.
(42) Joly-Pottuz, L.; Martin, J. M.; Dassenoy, F.; Belin, M.; Montagnac, G.; Reynard, B.; Fleischer, N. *J. Appl. Phys.* **2006**, *99*, 023524/1.
(43) Cizaire, L.; Vacher, B.; Le Mogne, T.; Martin, J. M.; Rapoport, L.; Margolin, A.; Tenne, R. *Surf. Coat. Technol.* **2002**, *160*, 282.
(44) Golan, Y.; Drummond, C.; Homyonfer, M.; Feldman, Y.; Tenne, R.; Israelachvili, J. *Adv. Mater.* **1999**, *11*, 934.
(45) Hu, X. G.; Hu, S. L.; Zhao, Y. S. *Lubr. Sci.* **2005**, *17*, 295.
(46) Greenberg, R.; Halperin, G.; Etsion, I.; Tenne, R. *Tribol. Lett.* **2004**, *17*, 179.
(47) Joly-Pottuz, L.; Dassenoy, F.; Belin, M.; Vacher, B.; Martin, J. M.; Fleischer, N. *Tribol. Lett.* **2005**, *18*, 477.
(48) Zhu, Y. Q.; Sekine, T.; Li, Y. H.; Fay, M. W.; Zhao, Y. M.; Poa, C. H. P.; Wang, W. X.; Roe, M. J.; Brown, P. D.; Fleischer, N.; Tenne, R. *J. Am. Chem. Soc.* **2005**, *127*, 16263.
(49) Zhu, Y. Q.; Sekine, T.; Li, Y. H.; Wang, W. X.; Fay, M. W.; Edwards, H.; Brown, P. D.; Fleischer, N.; Tenne, R. *Adv. Mater.* **2005**, *17*, 1500.
(50) Homyonfer, M.; Alperson, B.; Rosenberg, Y.; Sapir, L.; Cohen, S. R.; Hodes, G.; Tenne, R. *J. Am. Chem. Soc.* **1997**, *119*, 2693.
(51) Chen, J.; Kuriyama, N.; Yuan, H.; Takeshita, H. T.; Sakai, T. *J. Am. Chem. Soc.* **2001**, *123*, 11813.
(52) Zak, A.; Feldman, Y.; Lyakhovitskaya, V.; Leitus, G.; Popovitz-Biro, R.; Wachtel, E.; Cohen, H.; Reich, S.; Tenne, R. *J. Am. Chem. Soc.* **2002**, *124*, 4747.
(53) Imanishi, N.; Kanamura, K.; Takehara, Z. *J. Electrochem. Soc.* **1992**, *139*, 2082.
(54) Dominko, R.; Arcon, D.; Mrzel, A.; Zorko, A.; Cevc, P.; Venturini, P.; Gaberscek, M.; Remskar, M.; Mihailovic, D. *Adv. Mater.* **2002**, *14*, 1531.
(55) Afanasiev, P.; Rawas, L.; Vrinat, M. *Mater. Chem. Phys.* **2002**, *73*, 295.
(56) Mdleleni, M. M.; Hyeon, T.; Suslick, K. S. *J. Am. Chem. Soc.* **1998**, *120*, 6189.
(57) Bollinger, M. V.; Lauritsen, J. V.; Jacobsen, K. W.; Norskov, J. K.; Helveg, S.; Besenbacher, F. *Phys. Rev. Lett.* **2001**, *87*, 196803/1.
(58) Li, Y.-W.; Pang, X.-Y.; Delmon, B. *J. Phys. Chem. A* **2000**, *104*, 11375.

Table 1. Summary of Reaction Parameters (T_{ind}, T_{anneal}, and t_{anneal}) of the Two-Step Synthesis

MOCVD		annealing		
T [°C]	name	T [°C]	t [h]	name
450	WS_2 (450)	800	1	WS_2 (450/800-1)
450	WS_2 (450)	800	12	WS_2 (450/800-12)
550	WS_2 (550)	800	1	WS_2 (550/800-1)
650	WS_2 (650)	500	0.5	WS_2 (650/500-0.5)
650	WS_2 (650)	500	12	WS_2 (650/500-12)
650	WS_2 (650)	800	1	WS_2 (650/800-1)
650	WS_2 (650)	800	12	WS_2 (650/800-12)
650	WS_2 (650)	800	18	WS_2 (650/800-18)
750	WS_2 (750)	800	1	WS_2 (750/800-1)

Important questions emerging from this study were (i) how the product structure and particle size distribution are affected by the process parameters such as gas flow and reaction time and (ii) whether the two-step procedure, i.e., the formation of precursor nanoparticles by MOCVD and the subsequent formation of fullerene-type particles in a separate annealing step, might be simplified to a one-step procedure, thereby decreasing time and loss of material due to additional transfers, (iii) whether the reaction may be transferred in a 1:1 fashion to WS_2 particles considering the differences in the Mo–S and W–S phase diagrams,[59] and (iv) to which amount different stacking variants, i.e., the 2H- or the 3R-polymorph, of MoS_2 and WS_2 are formed. We report here a large-scale one-step synthesis of inorganic fullerene-type (IF) WS_2 nanoparticles by a MOCVD approach starting from tungsten hexacarbonyl and sulfur.

Experimental Section

Synthesis. In a first set of experiments hollow IF-WS_2 particles were synthesized using conditions similar to those employed for the synthesis of IF-MoS_2.[37] First, a MOCVD synthesis (e.g., at 450 °C, reaction time 2 h) was carried out, and the resulting material—collected from the inner walls of the reactor—was subjected to annealing (e.g., at 800 °C for 1 h under Ar) in a conventional tube furnace. Different synthesis temperatures (T_{ind}), annealing temperatures (T_{anneal}), and times (t_{anneal}) were studied as summarized in Table 1.

Previous results for an APCVD synthesis,[36] where hollow IF-MS_2 (M = Mo, W) particles were synthesized by the reaction of metal chlorides with sulfur in a tube furnace at 850 °C as well as our own experiments in the Mo/S system had shown that the reaction temperature was the most important parameter for the formation of closed nested structures. In order to test whether the *two-step reaction* could be simplified to a *single-step procedure*, a series of experiments was carried out in which the intermediate products were not isolated, but the temperature of the MOCVD reactor was varied during the reaction between 450 and 750 °C in steps of 100 °C.

For a comparison of the morphologies of IF-WS_2 obtained by the one-step process with those of the two-step procedure described by Etzkorn et al.,[37] reaction intermediates were also isolated and annealed under Ar at 500 and 800 °C for durations between 0.5 and 18 h. Relevant reaction parameters of the two-step process (T_{ind}, T_{anneal}, and t_{anneal}) are also summarized in Table 1.

In a typical MOCVD run 1.83 mmol (0.645 g) of $W(CO)_6$[60] (Aldrich, 99%) and 7.99 mmol (0.256 g) (4.32 mmol excess) of S (Alfa Aesar, 99.5%+, -100 mesh, sublimed) were weighed in and inserted into the setup under constant Ar flow. While the precursors $W(CO)_6$ and S were heated at 150 and 250 °C, respectively, for all experiments, the temperature of the hot zone was varied from 450 to 750 °C in steps of 100 °C for different experiments. A constant reaction time of 2 h was used for the MOCVD step of all experiments.

Characterization. *Electron Microscopy.* The products were characterized using high-resolution scanning electron microscopy (HRSEM) (LEO 1530 field emission SEM, 6 kV extraction voltage) and transmission electron microscopy (TEM) carried out on a Philips EM420 instrument with a twin lens and a Philips CM12 with a twin lens at an acceleration voltage of 120 kV. High-resolution images were taken with a Philips FEI TECNAI F30 ST electron microscope (field-emission gun, 300 kV extraction voltage) equipped with an Oxford EDAX (energy-dispersive X-ray) spectrometer with a Si/Li detector and an ultrathin window for elemental analysis. Samples for TEM measurements were prepared from ethanolic suspensions of the samples. Three drops of an ultrasonicated suspension were administered on a Cu grid coated with FORMVAR polymer and an amorphous carbon layer.

X-ray Powder Diffraction. X-ray diffraction patterns (XRD) were recorded using a Bruker AXS D8 Discover powder microdiffractometer (Cu Kα radiation, graphite monochromator) equipped with a 2D HiStar detector. Profiles were fitted with TOPAS 3.0P[61] using SPVII profile functions in order to elucidate crystallinity and crystal size. Phase analyses were performed by means of Rietveld refinements based on the fundamental parameter approach and the structure models given in ref 62 using TOPAS Academic.[63]

Results and Discussion

In the following section, the results of the single-step MOCVD process will be described and compared with those of the two-step procedure. Our discussion will focus only on the reaction temperature. Variations of Ar carrier gas flow and reaction time turned out to play only a minor role. For the two-step process (section 2) various experimental conditions were used (see Table 1), but the discussion is restricted to the pristine WS_2 (650) and the annealed WS_2 (650-800/12) samples.

1. Filled IF-WS_2 Particles by in Situ Heating of the Reaction Intermediates: Single-Step Process. *Influence of the Reaction Temperature in the Induction-Heated Zone.* The MOCVD synthesis of WS_2 from $W(CO)_6$ and S was carried out at four different temperatures of the induction heated zone (T_{ind} = 450, 550, 650, 750 °C) in order to study the role of temperature for the formation of closed-shell structures in a single step. Deposition of a black product started on the cold parts at the inside of the inner cylinder, i.e., above the heating zone of the induction furnace, about

---

(59) Massalski, T. B.; Okamoto, H.; Subramanian, P. R.; Kacprzak, L. *Hf-Re to Zn-Zr*, 2nd ed.; ASM International: Materials Park, OH, 1990; Vol. 3, p 2664.

(60) $W(CO)_6$ is toxic. It is hazardous because of the release of poisonous carbon monoxide. CO forms explosive mixtures with air. (Explosion limits: 12.5–74%, autoignition temperature 620 °C). Therefore, oxygen-free atmosphere has to be assured throughout the experiment.

(61) *TOPAS*, 3.0P; Bruker AXS: Karlsruhe, 2003.

(62) Schutte, W. J.; De Boer, J. L.; Jellinek, F. *J. Solid State Chem.* **1987**, *70*, 207.

(63) Coelho, A. *TOPAS Academic*, 1.0; Bruker AXS.

(64) For the sake of clarity only (002) will be used to design the 2H-(002)/3R-(003) reflection hereafter.

(65) Dunn, D. N.; Seitzman, L. E.; Singer, I. L. *J. Mater. Res.* **1997**, *12*, 1191.

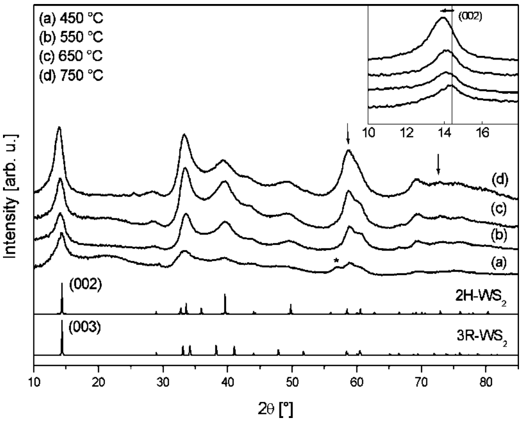

Figure 1. XRD traces of samples synthesized at 450 (a), 550 (b), 650 (c), and 750 °C (d) and the calculated diffraction patterns of 2H- and 3R-WS_2. A magnification of the (002) reflection is displayed in the inset. The arrows mark the (200) and (211) reflection of α-W (JCPDF Card No. 4-806). One unidentified reflection is indicated with an asterisk (*).

Table 2. Summary of (002) Reflection Profile Parameters (Values for Samples Synthesized at 450, 550, 650, and 750 °C Are Given)

		fwhm [deg]				
T [°C]	2θ [deg]	left	right	sum	d [Å]	lattice exp[a] [%]
450	14.3068	1.1711	0.8518	2.0229	6.19	0.4
550	14.1579	0.9970	0.7534	1.7504	6.25	1.5
650	14.1124	0.7952	0.7149	1.5101	6.27	1.8
750	13.9647	0.8639	0.6555	1.5194	6.34	2.9

[a] Lattice expansion in relation to the bulk d_{002}.

10 min after the final reaction temperature was reached. For T_{ind} > 650 °C a metallic product was observed at the outside of the inner cylinder as well as in the lower inner part. The yield of WS_2 nanoparticles increased with increasing reaction temperature T_{ind}.

X-ray Powder Diffraction. X-ray diffractometry was used to determine the overall composition and structure of the products. It requires the availability of material in sufficient amount and purity, and it is used here for the first time in a systematic fashion for the structural analysis of chalcogenide nanoparticles. X-ray diffraction patterns of all samples (see Figure 1) indicate the presence of tungsten disulfide (JCPDF Card No. 8-237 and 35-651) independent of the choice of reaction parameters.

The reflection broadening due to particle size effects prevents a clear distinction whether the 3R modification of WS_2 is present in addition to the 2H phase. The results of Rietveld refinements indicate that the 3R variant predominates (~60–80%) while the 2H variant is the minority component (Figure S1, Supporting Information). A tungsten impurity can be identified by its (200) and (211) reflection (indicated by arrows in Figure 1) for samples synthesized at $T_{ind} \geq 550$ °C. As the synthesis temperature T_{ind} is increased from 450 to 750 °C, several tendencies can be noted: (1) an increase in intensity especially for the (002) reflection, (2) a decrease in its peak width (see inset Figure 1 and fwhm values in Table 2), (3) a linear increase in the d_{002} values (e.g., decrease in 2θ values, see inset Figure 1) and their variance as displayed in Figure 2, and (4)a decrease in peak asymmetry up to $T_{ind} \leq 650$ °C and an increase for $T_{ind} =$ 750 °C (see ratio of left and right contribution to fwhm in Table 2).

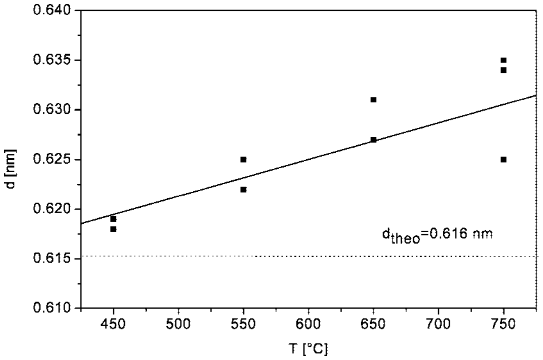

Figure 2. Lattice expansion monitored by means of the d_{002} values of samples synthesized at 450, 550, 650, and 750 °C. A linear fit is displayed as a black line.

The (002) reflection is indicative of the stacking of the WS_2 layers. Its presence even in the 450 °C samples shows that a reaction between $W(CO)_6$ and S has taken place, resulting in the formation of small regions of stacked WS_2 layers. For higher reaction temperatures the order and the crystallinity of the products improve continuously. This is reflected in the increasing intensity, sharpness, and symmetry of the (002) reflection shown in the inset of Figure 1. Another indicator are the decreasing fwhm values and the ratio of left and right contributions of the fwhm compiled in Table 2.

All d_{002} values (see Table 2), i.e., the stacking distances, are significantly enlarged as compared to the bulk material. This has also been observed for other IF structures (such as MoS_2 synthesized in a fluidized bed reactor[66]) and can be attributed to a lattice expansion due to curvature of the sheets or defects. The increase in lattice expansion for samples synthesized at higher temperatures is due to an increased amount of curved structures with decreasing radius. A detailed discussion will be given below.

Electron Microscopy. While the X-ray diffractometry provides information concerning the average structure of a bulk sample, electron microscopy gives a local view of the particle structure and particle size distribution. It cannot give a reliable estimate of the sample homogeneity. Figure 3 shows representative TEM micrographs of samples synthesized at (a) 450, (b) 550, (c) 650, and (d) 750 °C. All samples consist of network-like agglomerates of small particles with diameters ranging from about 10 to 150 nm. Two sorts of particles can be distinguished according to their diameters and shapes. The fraction of whisker-like particles with the smallest diameters (~10 nm) (referred to as S-type particles in the sequel) contains irregular shaped but rather spherical particles, which are often interconnected in a manner observed for molten metals. In contrast to the S-type particles obtained in the case of MoS_2 and $MoSe_2$[37] the layers are straight and not curved. This increased stability of the WS_2 layers may be the result of stronger van der Waals interactions between the slabs due to the higher polarization of S by Mo compared to W. This observation would also be consistent with the lower reactivity of WS_2 in intercalation

---

(66) Margolin, A.; Rosentsveig, R.; Albu-Yaron, A.; Popovitz-Biro, R.; Tenne, R. *J. Mater. Chem.* **2004**, *14*, 617.

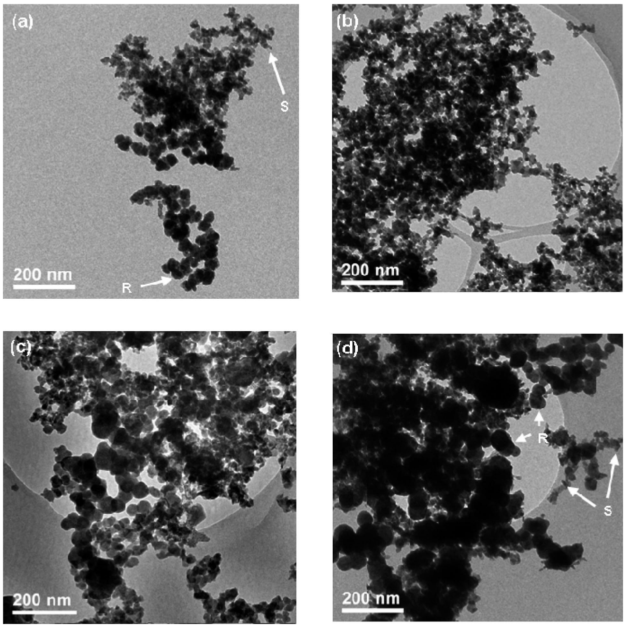

Figure 3. TEM overview images of samples synthesized at 450 (a), 550 (b), 650 (c), and 750 °C (d). The arrows in (a) and (d) highlight irregularly shaped small S-type particles and bigger spherical R-type particles.

reactions.[67] The second fraction of particles with spherical shape (round/R-type particles) exhibits mean diameters between 25 and 200 nm. High-resolution images show faceting due to nonconnected layer "packages".

Samples Prepared at 450 °C. In samples synthesized at 450 °C the S-type particles are predominant, with a small portion of R-type particles (Figures 3a and 4e). A high-resolution (HRTEM) image of the S-type particle agglomerate is provided in Figure 4a. It confirms the small coherence length that has been proposed from the XRD measurements due to (i) the presence of partly amorphous material, (ii) the small number of WS_2 layers (up to 7), and (iii) the small particle size (ca. 10 nm in length) of the crystalline parts. The *d*-spacing of 0.640 nm corresponds to a lattice expansion of 3.8%.

Samples Prepared at 550 °C. Figure 3b shows the overview TEM micrograph of a sample synthesized at 550 °C. It contains S- and R-type particles as found for the reaction at 450 °C, but the fraction of R-type particles has increased. In HRTEM studies more layered particles were observed compared to samples prepared at lower (450 °C) temperature.

The S-type particles (Figure 4b) are made up of 4–10 layers of about 10 nm in length. For some of them the length of the outer layers is smaller than that of the inner layers, which leads to a spherical appearance of the particles even though the individual layers are not bent. A decrease of the interlayer spacing to 0.633 nm (2.8% lattice expansion) can be observed. The R-type particles consist of fragments containing 4–6 curved layers in a stacked arrangement. These fragments are arranged around an amorphous core in a spherical fashion. They are not intergrown, and their overall appearance resembles that of an onion-type structure (Figure 4f).

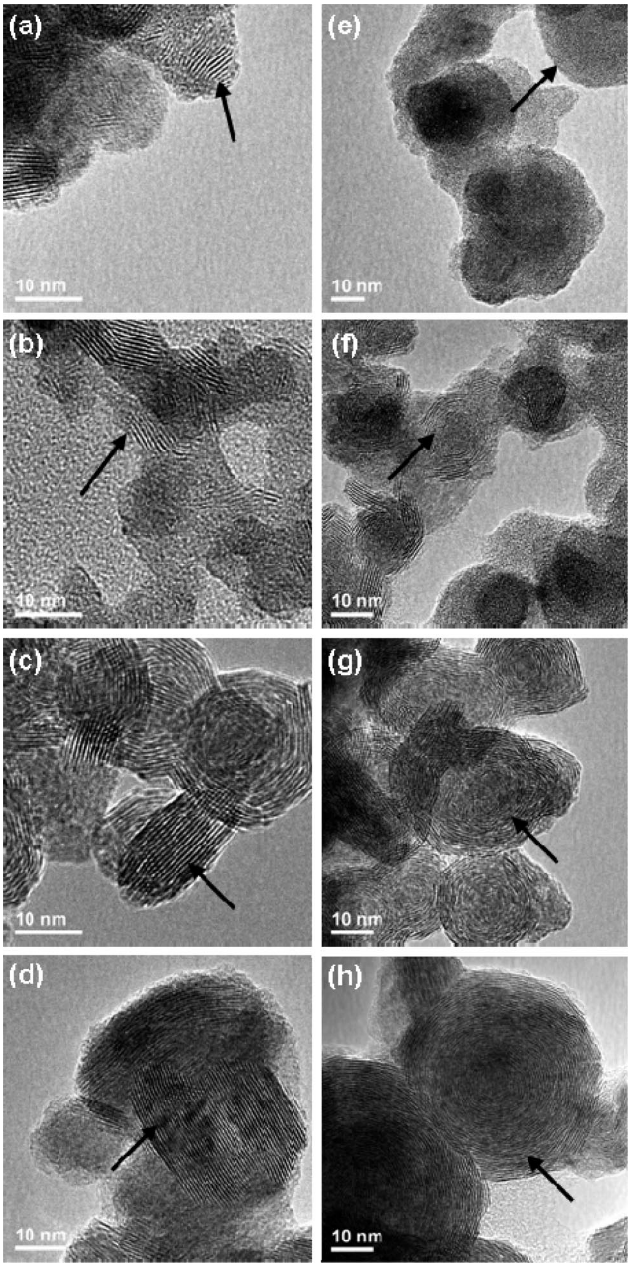

Figure 4. HRTEM images of S-type (a–d) and R-type (e–h) particles in samples synthesized at 450 (a/e), 550 (b/f), 650 (c/g), and 750 °C (d/h).

The interlayer separation for these fragments is 0.651 nm (5.7% lattice expansion). We note that the interlayer distance varies not only between two different pairs of layers but also for an individual pair, especially in curved layers, whereas in S-type particles the interlayer distance remains constant. This points to a larger number of defects (namely edge dislocations) and stacking faults for the curved structures. As a matter of fact, we observe a higher defect concentration for the curved structures in HRTEM studies. Thus, the relatively large lattice expansion reflected in a large d_{002} value (from X-ray studies) is caused not only by the curvature but also by a large number of defects present in these particles.

Samples Prepared at 650 °C. Increasing the reaction temperature leads to enhanced particle growth through the formation of larger sheets and a higher degree of agglomeration by sheet stacking (Figure 3c). S-type particles (Figure

---

[67] Etzkorn, J.; Rocker, F., Personal communication.

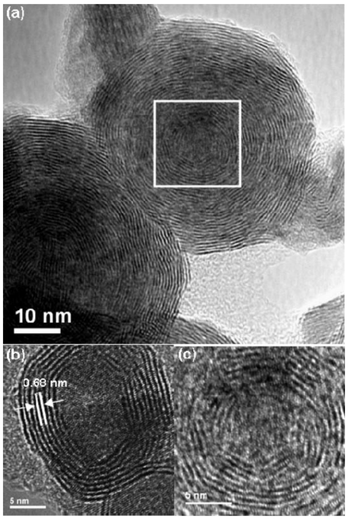

Figure 5. Filled (a) and hollow (b) onion-like structures, obtained from a WS_2 (750) and a WS_2 (650/800-12) sample, respectively. Background filtered IFFT of the central part (white square in (a)) of the filled onion-like structure is given in (c).

4c) exhibit up to 18 layers with sheet diameters of ~20 nm and an average interlayer spacing of 0.636 nm (3.3% lattice expansion). The amount of S-type particles decreases with increasing temperature, while the number of R-type particles (Figure 4g) increases. In R-type particles the lateral growth of the layered fragments leads to particle intergrowth and therefore to the formation of closed structures with up to 10 layers with $d_{002} = 0.654$ nm, corresponding to a lattice expansion of 6.2%. The large number of defects resulting from the temperature increase suggests that fullerene-type particles may be formed at higher temperatures because a sufficiently strong curvature is induced through the formation of rhomboidal or triangular defects of the otherwise flat 2D MQ_2 sheets.

Samples Prepared at 750 °C. When the reaction temperature was raised to 750 °C, onion-shell-like structures with a large number (up to 25) of layers *with a filled core* were obtained (Figure 5a). Their structure differs from that of the particles obtained by the two-step procedure (vide infra) in that the onion shell contains only a few *well-ordered layers around a hollow core* (Figure 5b,c). Filled core particles have already been synthesized by several groups, the core being a material similar to[33] or different from MS_2,[17,32,68] e.g., from remaining oxide due to incomplete sulfurization.[69] Our filled onion-shell-like particles still exhibit some edge dislocations, but significantly less than the particles synthesized at 650 °C. The average *d*-spacing of 0.656 nm indicates a lattice expansion of about 6.5%.

In most of the onion-like particles no lattice fringes can be observed in the central part (~3 nm), but the contrast in low-resolution TEM images is stronger than that for the center of the hollow particles found after annealing. This indicates that the particles are filled either with amorphous material or yet some sheets for which the higher thickness of the particles at the center of the particle prevents the detection of the lattice fringes of crystalline material. We also observe the formation of S-type particles (in small amounts). The numbers of layers ($d_{002} = 0.640$ nm $= 3.8\%$ lattice expansion) and concomitantly their size has increased.

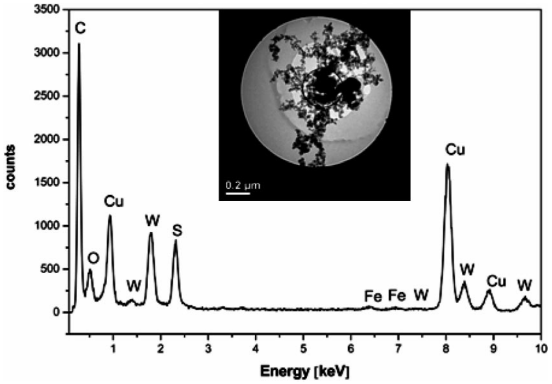

Figure 6. EDX spectrum of a 450 °C sample. The analyzed area is marked in the corresponding TEM image in the inset. W(L):S(K) ratio is determined as 1:2.

In summary, increasing reactor temperatures lead to increased crystallinity. There is no specific trend in the evolution of the *d* values of the S-type particles whereas for the R-type particles an increase of the lattice expansion can be observed. This is in line with the observed shift of the 2θ values of the (002) reflection to lower values (higher d_{002} values) for the R-type particles.

The increasing peak asymmetry for the WS_2 (750) sample can be explained by the formation of nearly closed onion-like structures and therefore a higher amount of curvature and strain. The outward-in direction of the crystallization process (cf. growth mechanism) allows the formation of the innermost shells, i.e., the most bent ones, only at higher temperatures, and therefore increasing the total amount of strain. This finding would also explain the increase in the inner strain when the reaction temperature is raised to 750 °C.

Figure 6 shows a representative EDX spectrum of a sample synthesized at 450 °C. The overall W:S ratio is 1:2. The S-type particles are typically more tungsten-rich than the R-type particles. Increasing the reaction temperature leads to a depletion in the sulfur content especially for the R-type particles, in harmony with thermodynamic predictions.

Scanning electron microscopic studies confirm the network-like morphology of all samples regardless of the reaction temperature. Figure 7 displays an overview of a WS_2 (550) sample where the sponge-like structure is clearly visible. Samples obtained at different reaction temperatures look similar, except for the WS_2 (750) sample, which appears slightly denser.

High-resolution SEM imaging (see inset of Figure 7) allows the distinction between spherical R-type and more irregular shaped S-type particles. We note that the S-type particles imaged by HRSEM must be regarded as an ensemble of the S-type particles as described in the TEM section because the resolution of HRSEM is not high enough to clearly visualize the individual crystallites. The resolution limit may also be the reason why a quantification of the R/S-

---

(68) Si, P. Z.; Zhang, M.; Zhang, Z. D.; Zhao, X. G.; Ma, X. L.; Geng, D. Y. *J. Mater. Sci.* **2005**, *40*, 4287.

(69) Sloan, J.; Hutchison, J. L.; Tenne, R.; Feldman, Y.; Tsirlina, T.; Homyonfer, M. *J. Solid State Chem.* **1999**, *144*, 100.

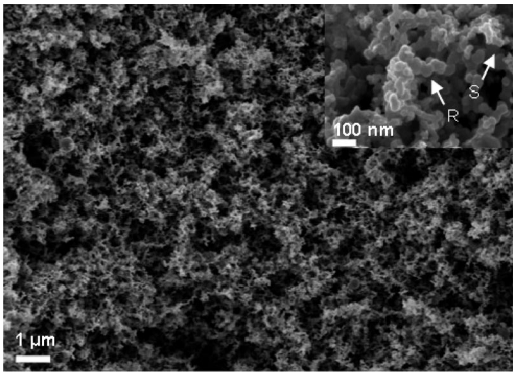

Figure 7. HRSEM image of a sample synthesized at 550 °C. S- and R-type particles are marked with arrows.

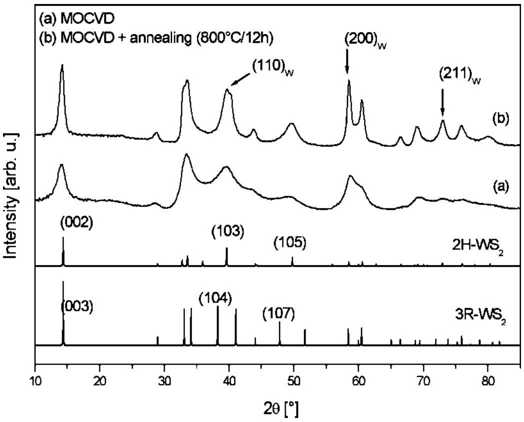

Figure 8. XRD patterns of a sample synthesized at 650 °C before (a) and after (b) annealing at 800 °C for 12 h. The arrows indicate the (110), (200), and (211) reflections of α-W. Simulated diffraction patterns of 2H- and 3R-WS_2 are given for comparison.

type particle ratio is not possible from these measurements. From a qualitative point of view none of the two particle types is predominant, and no distinctive change in their proportion can be observed. The average diameter of the R-type particles increases from 30 to 40 nm with increasing temperature.

2. Hollow IF-WS_2 Particles by Isolating and Subsequent Annealing of the Reaction Intermediates: Two-Step Process. The synthesis of WS_2 via MOCVD at $T_{\mathrm{ind}} = 650$ °C for 2 h resulted in a black deposit at the inside of the inner glass cylinder that could be easily removed with a spatula. The yield was in the 100 mg range. This comparably large amount of material and the specially equipped micro-diffractometer allowed us to employ X-ray diffractometry to obtain information about the bulk composition and structure of the samples before (Figure 8a) and after (Figure 8b) annealing.

X-ray Powder Diffraction. X-ray diffractometry (see Figure 8) shows a high crystallinity of the nanoparticles. In contrast to the bulk material, the reflections profiles are broadened due to particle size effects and shifted toward lower scattering angles. This is in accordance with the general finding of increasing lattice distances in curved materials. As a consequence of the reflection profile broadening, a clear distinction between the 2H- and 3R-polymorphs is technically inappropriate.

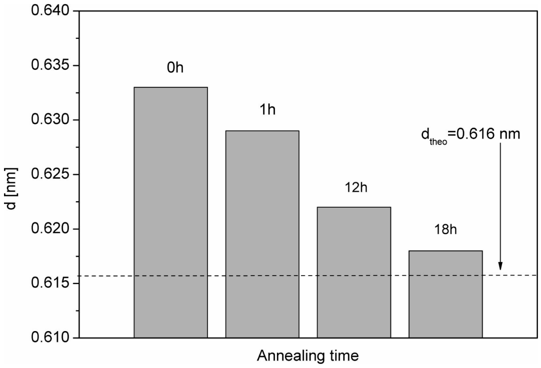

Figure 9. Development of d_{002} values obtained from XRD as a function of annealing time for a WS_2 (650) sample.

The extent of peak broadening is reduced for the annealed sample. This may be attributed to a crystallization process where the thermodynamically favored 2H-polymorph is formed. The reduction of the d_{002} value for annealed samples can be observed for all samples regardless of their original synthesis temperature T_{ind}. The effect is more pronounced (reduction to a lattice expansion of 0.3%, i.e., the value of the bulk material is nearly reached) for longer annealing times (18 h, see Figure 9).

Electron Microscopy. High-resolution scanning electron microscopy (HRSEM) revealed the presence of agglomerates of spherical particles with diameters of about 30 nm. In addition to these spherical particles, the annealed sample exhibits a minor portion (10–20%) of needle-like particles of 10–20 nm in diameter and 50–more than 100 nm in length (see Figure S2, Supporting Information).

Figure 10 displays (HR)TEM images of samples synthesized at 650 °C before (a) and after (b) annealing. All samples consist of network-like agglomerates of small particles. Samples *without further thermal treatment* exhibit two types of particles: small irregular shaped particles (S) with visible WS_2 layers and a significant amount of bigger (>50 nm) spherical particles (R) with lattice fringes at the outer edges. The values for the *d*-spacings range from 0.62 to 0.66 nm (corresponding to a lattice expansion of 0.6 to 7.1%), confirming the large variation of interlayer distances already observed by XRD.

The *annealed sample* consists of two types of particles: nanowhiskers (N) and hollow nested onion-like (O) particles in about equal quantities (Figure 10b). The nanowhiskers are about 10–15 nm in diameter with an aspect ratio ranging from 1.9 to 6.0. As can be seen in the high-resolution TEM image (Figure 10b), they consist of highly crystalline, well-stacked layers with an average interlayer distance of $d = 0.64$ nm (3.9% lattice expansion). This value is only slightly larger than the one obtained by XRD ($d = 0.622$ nm, ~1% lattice expansion). If defects occur (in form of edge dislocations), they tend to be close to the tips of the nanowhiskers. All whiskers grow perpendicular to *c*, e.g., the stacking direction of the WS_2 slabs.

The onion-like structures vary from 15 to 100 nm in size. Onion-like structures of 15–30 nm are mainly spherical consisting of 3–10 "shells" of WS_2 layers *around a hollow core*. Bigger onion-like structures with diameters between 30 and 100 nm are mostly elongated or consist of "onions

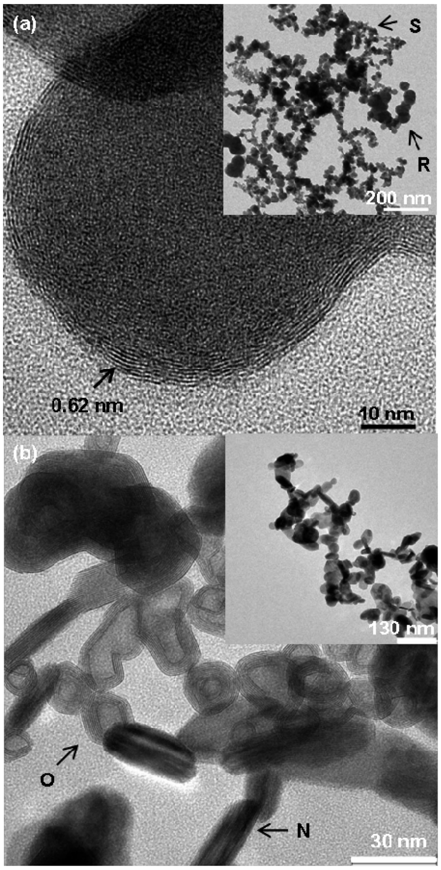

Figure 10. HRTEM images of a sample synthesized at 650 °C before (a) and after (b) annealing for 12 h at 800 °C. A corresponding overview TEM image is given in the inset.

in an onion structure" that can have 20 and more shells in total. The concave structures are obtained either by bending of the layers or by polyhedral joints of layer fragments with angles <180° (often ~130°–145°), resulting in the formation of faceted structures. The average d_{002}-spacing of 0.67 nm corresponds to a lattice expansion of 9%, a value significantly higher than d_{002} obtained by XRD. As the annealed samples exhibit well-ordered and well-stacked layers in comparison to the nonannealed samples, this lattice expansion has to be attributed to curvature (especially of the small diameter onions) and not to defects.

The decrease in lattice expansion for the annealed sample compared to the pristine material can be explained by defect healing. An alternative explanation is as follows: the (002) reflection close to the ideal bulk value contains contributions from (i) needle-like nanocrystals with straight layers and a relatively small d_{002} value and (ii) those parts of the onion-like structures which are built up from straight layered fragments in a faceted manner. Because the XRD pattern is the superposition of contributions from all particles, that part of the sample with highly ordered, straight layered particles will lead to a reduced overall d_{002} value. On the other hand, the contributions from of onion-like structures (with curved layers) are superimposed and should lead to a lattice expansion as well as to strain (peak asymmetry, see fwhm ratio in Table 2). Because the fullerene-like structures are hollow, very small radii do not occur. Therefore, less lattice expansion is present. In summary, the healing of defects and the formation of straight layered particles outweighs the effect of curvature on the evolution of the d_{002} values.

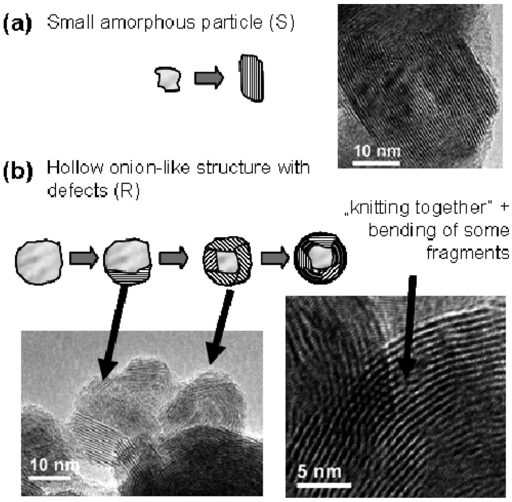

Figure 11. Formation of S-type (a) and R-type (b) particles: scheme and TEM images.

In order to answer the question whether the faceted or the bent structures are the thermodynamically favored forms of WS_2, reactions were carried out with longer annealing times at 800 °C. After 18 h of annealing, both particle types are still present with none of it prevailing. Bending or faceting appears to depend on the radius of the particle as already observed for NbS_2 onion-like particles.[22] At the inner parts faceted growth is observed more often whereas the outer layers tend to be bent.

In summary, *hollow IF-WS_2 particles could be obtained from a two-step synthesis* using conditions similar to those reported for the synthesis of MoS_2 or $MoSe_2$. In situ HRTEM heating studies indicate that the ratio of onion-like structures to needles is dependent on the morphology of the product before heating (see the following section) and not on the annealing conditions.

3. Growth Mechanism of the in Situ Heated Product. TEM studies of the in situ heated product obtained from the one-step reaction reveal the formation of two types of particles (S + R). The size of both types of particles increases and the crystallinity improves when the reaction temperature is raised from 450 to 750 °C. A feasible growth mechanism of these particles is depicted in Figure 11 and discussed in the following section.

In the first reaction step the precursors $W(CO)_6$ and S_8 are heated in a continuous Ar flow. At 250 °C the sulfur precursor has passed its melting point, and a constant vapor pressure has built up. Heating the precursor $W(CO)_6$ to 150 °C results in its decomposition according to

$$W(CO)_6 \xrightarrow{\Delta T} W + 6CO \qquad (1)$$

The decomposition/evaporation products are transported with the Ar carrier gas flow to the central part of the reactor. In the upper part of the reactor the carrier gas streams containing W, CO, and S_g mix intimately to form a homogeneous amorphous mixture, a reaction intermediate for the preparation of nanoparticles or extended solids of the binary phase.

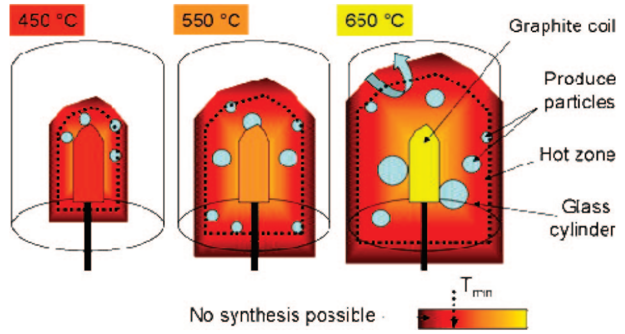

Figure 12. Schematic representation of the hot zone of the reactor around the graphite coil. A dotted line represents the minimum temperature needed for particle growth.

Nucleation of WS_2 is induced and controlled by the temperature. It occurs in the hot zone of the induction furnace around the graphite coil if $T > T_{min}$ (as W and S are highly dispersed T_{min} will be lower than for the bulk synthesis of WS_2 out of the elements). The extension of the hot zone is small for low T and increases with increasing T (Figure 12).

The key factor for the formation of particles with different sizes would be the difference in the retention times of the particles in the growth region, i.e., the region with $T > T_{min}$. S-type particles appear to traverse only a short trajectory through the growth region. These particles can be trapped by contact with the glass cylinder, which leads to their irregular shape. Particles experiencing a longer trajectory through the growth region are more likely to form aggregates (Figure 11b). The longer reaction time also enables these particles to adopt the energetically preferred spherical equilibrium morphologies. The higher the reaction temperature, the more extended the growth region and therefore the more different the trajectories. This leads to a less controllable particle size but a higher amount of R-type particles.

This growth model would explain (i) the formation of two different particle types, (ii) the increasing amount type R particles, (iii) their increasing size with increasing reaction temperatures, (iv) the increasing variance of the d values (see Figure 2) for higher temperatures, and (v) the observed variance in the crystallinity.

In HRTEM studies we find incipient crystallization at $T_{ind} = 450$ °C for the S-type particles, whereas the R-type particles are still amorphous. This suggests that for the partly amorphous small particles crystallization is favored, whereas for the larger spherical particles surface/defect minimization by particle intergrowth is dominant. At elevated reaction temperatures ($T > 550$ °C) the crystallization of the R-type particles starts at the outer boundaries. For particles beyond a critical size crystallization starts simultaneously at several sites of the surface, and several layered fragments start to intergrow and to enclose an amorphous core (see Figure 11b). As a result, facetted particles are formed on the basis of interconnected fragments with numerous defects at their boundaries. The major portion of these fragments contains planar layers that are still unbent. Only at higher reaction temperatures (>650 °C) a bending of these layers and an associated formation of defects is observed. In addition, multinuclear particles have been observed (see Figure 13).

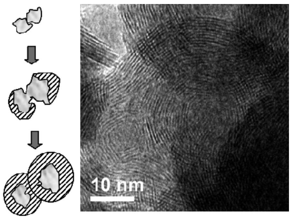

Figure 13. Formation of a binuclear particle (left: schematic representation; right: corresponding HRTEM image).

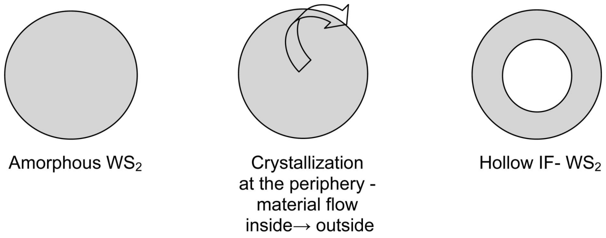

Figure 14. Scheme illustrating the formation of hollow IF-WS_2 nanoparticles in the two-step process.

4. Why Are the Particles Obtained from the Two-Step Reaction Hollow? Growth Mechanism of the Annealed Intermediate. Conceptually, the formation of solid-state compounds can be broken down into two key steps: the interdiffusion of the reactants and the nucleation/crystallization of products. Since IF- and NT-type WS_2 represent binary nonequilibrium phases, the synthetic goal is to gain kinetic control of the reaction by eliminating diffusion as a rate-limiting step. This leaves nucleation, a kinetic phenomenon dependent upon overcoming a reaction barrier, as the crucial reaction step. A homogeneous, amorphous mixture of the components is an ideal reaction intermediate for the preparation of extended solids. The interdiffusion of the reactants is driven by the large negative heat of mixing, and only the growth of this amorphous mixture would be diffusion-controlled. For particles with diameters of approximately 10–20 nm, diffusion is completed during the formation of this mixture, leaving nucleation as the rate-limiting step in the formation of the ordered "crystalline" solid. When the amorphous particles are heated, WS_2 starts to nucleate and grows until its growth exhausts one of the reactants within the particle volume or until the particle boundary is reached (see Figure 14). Since intraparticle growth is preferred over interparticle growth, an additional size restriction is imposed by the diameter of the particles containing the amorphous mixture.

This transformation from the amorphous mixture to IF-WS_2 starts at the particle boundaries, where the surface reactivity is highest; i.e., an ordered WS_2 shell is formed around the amorphous core. The crystallization proceeds *outside-in*. As the density of the "crystalline" IF-WS_2 is larger than that of the amorphous core, there is a mass transfer to the particle boundary while the interior of the particle is depleted. The driving force for the mass transfer is a concentration gradient of WS_2 due to the compactization. After the formation of a shell consisting of 10–20 WS_2 layers the material supply from the interior of the particle is so small that the material flow to the particle boundary ceases. As a result, the particle remains empty.

The associated transformation from an amorphous to a more dense crystalline material is reminiscent of a 3D analogue of the so-called "coffee stain effect" (where ring-like deposits are obtained on a 2D support upon evaporation of a solvent drop).[71,72] An outward flow of material in a crystallizing spherical particle is produced when the outer particle boundary is pinned so that material compacting at the edge of the sphere must be replenished by a mass flow from the interior.

Alternatively, the formation of the hollow IF particles may be related to the Kirkendall effect.[73] This effect arises when the interdiffusion between two solids is realized via vacancy transport and an asymmetry of the related diffusion rates occurs, which finally results in the formation of pores. This method for the fabrication of hollow particles starting from an amorphous precursor has a number of advantages. For example, the required voids need not be produced beforehand. This, in the end, may allow the fabrication of three-dimensional nanostructures of complex shape. In addition, the formation of nanoparticles with large aspect ratios may be obtained, and the method can be scaled up to produce large volume quantities useful for various applications.

Summary and Conclusion

We have reported on a simplified MOCVD approach for the synthesis of MS_2 which avoids the isolation and subsequent annealing of the reaction intermediate. Eliminating of the annealing step by heating the reaction zone of the reactor leads to two types of particles, i.e., small irregular (S-type) and bigger spherical (R-type) particles. The spherical particles can be converted to filled onion-like particles. The crystallinity and the size of the particles (i.e., the number of layers per particle and the diameters of the individual WS_2 sheets) increase with increasing reaction temperature. EDX analyses show a W:S ratio of 1:2. The optimum processing temperature for the synthesis of filled fullerene-like structures was 750 °C. In contrast, *the two-step process* comprising an isolation and subsequent separate annealing of the reaction intermediate leads to the formation of hollow nanoparticles. A growth mechanism was proposed to explain the formation of two different types of onion-type particles in the by the one-step and the two-step approach. Thus, the MOCVD approach allows the selective synthesis of hollow or filled onion-type WS_2 nanoparticles. It can be applied for a variety of different binary and even ternary layered compounds under environmentally friendly conditions with the prospect of easy upscaling, e.g., by using microreactor techniques.

Acknowledgment. We gratefully acknowledge the help of G. Glasser and M. Messerschmidt for HRSEM and SEM measurements. We also thank R. Jung-Pothmann for X-ray diffraction measurements. Julien Pansiot and Jérôme Kieffer are recipients of an Erasmus fellowship of the European Community. Microscopy equipment is operated by the electron microscopy center, Mainz (EMZM), supported by the Johannes Gutenberg-University and the Max Planck-Institute for Polymers (MPI-P). This research was supported by the Deutsche Forschungsgemeinschaft (DFG/SFB625) and the materials science center (MWFZ) in Mainz.

Supporting Information Available: Rietveld refinement of a WS_2 sample and details concerning the powder diffractometry and Rietveld refinements and high-resolution SEM image of a WS_2 (650/800-12) sample. This material is available free of charge via the Internet at http://pubs.acs.org.

CM070938S

---

(70) Meyer, K. *Physikalisch-chemische Kristallographie*; Dt. Verl. für Grundstoffindustrie: Leipzig, 1977; p 368.

(71) D'Souza, S. M.; Alexander, C.; Carr, S. W.; Waller, A. M.; Whitcombe, M. J.; Vulfson, E. N. *Nature (London)* **1999**, *398*, 312.

(72) Loges, N.; Therese, H. A.; Graf, K.; Nasdala, L.; Tremel, W. *Langmuir* **2006**, *22*, 3073.

(73) (a) Kirkendall, E. O.; Thomassen, L.; Upthegrove, C. *Trans. AIME* **1939**, *133*, 186. (b) Kirkendall, E. O. *Trans. AIME* **1942**, *147*, 104. (c) Smigelskas, A. D.; Kirkendall, E. O. *Trans. AIME* **1947**, *171*, 130.